NeuroImage 187 (2019) 154–165

Contents lists available at ScienceDirect

NeuroImage

journal homepage: www.elsevier.com/locate/neuroimage

A novel perspective to calibrate temporal delays in cerebrovascular reactivity using hypercapnic and hyperoxic respiratory challenges

Allen A. Champagne [a,1], Alex A. Bhogal [b,2], Nicole S. Coverdale [a,1], Clarisse I. Mark [a,3], Douglas J. Cook [a,c,*]

[a] Centre for Neuroscience Studies, Queen's University, Kingston, ON, Canada
[b] Department of Radiology, University Medical Center Utrecht, Utrecht, The Netherlands
[c] Department of Surgery, Queen's University, Kingston, ON, Canada

ARTICLE INFO

Keywords:
Cerebrovascular reactivity
Temporal delays
Hypercapnia
Hyperoxia
BOLD signal
Cerebral blood flow
RIPTiDe

ABSTRACT

Redistribution of blood flow across different brain regions, arising from the vasoactive nature of hypercapnia, can introduce errors when examining cerebrovascular reactivity (CVR) response delays. In this study, we propose a novel analysis method to characterize hemodynamic delays in the blood oxygen level dependent (BOLD) response to hypercapnia, and hyperoxia, as a way to provide insight into transient differences in vascular reactivity between cortical regions, and across tissue depths. A pseudo-continuous arterial spin labeling sequence was used to acquire BOLD and cerebral blood flow simultaneously in 19 healthy adults (12 F; 20 ± 2 years) during boxcar CO_2 and O_2 gas inhalation paradigms. Despite showing distinct differences in hypercapnia-induced response delay times ($P < 0.05$; Bonferroni corrected), grey matter regions showed homogenous hemodynamic latencies ($P > 0.05$) once calibrated for bolus arrival time derived using non-vasoactive hyperoxic gas challenges. Longer hypercapnic temporal delays were observed as the depth of the white matter tissue increased, although no significant differences in response lag were found during hyperoxia across tissue depth, or between grey and white matter. Furthermore, calibration of hypercapnic delays using hyperoxia revealed that deeper white matter layers may be more prone to dynamic redistribution of blood flow, which introduces response lag times ranging between 1 and 3 s in healthy subjects. These findings suggest that the combination of hypercapnic and hyperoxic gas-inhalation MRI can be used to distinguish between differences in CVR that arise as a result of delayed stimulus arrival time (due to the local architecture of the cerebrovasculature), or preferential blood flow distribution. Calibrated response delays to hypercapnia provide important insights into cerebrovascular physiology, and may be used to correct response delays associated with vascular impairment.

Introduction

Mapping of cerebrovascular reactivity (CVR) with MRI during the application of a vascular stimulus can be used to identify vascular impairment associated with conditions such as Moyamoya (Han et al., 2011) and steno-occlusive disease (Sam et al., 2014). Increasing the partial pressure of arterial carbon dioxide gas (P_aCO_2), a state defined as hypercapnia, serves as a potent vasoactive agent, whereby arterial CO_2 reacts with blood water to form carbonic acid and an increase in free hydrogen ion concentration. This leads to a decrease in blood pH (Kontos, 1977), affecting ATP- and voltage-gated potassium channels lining the arterial endothelial surface and leading to hyperpolarization of endothelial cells (Lindauer et al., 2003). Hypercapnia mediated changes in local membrane potential propagate to adjacent smooth muscle cells, causing smooth muscle relaxation, via closure of calcium channels, and a concomitant reduction in intracellular calcium (as reviewed in Glodzik et al., 2013; Brian, 1999). The resulting vasodilation leads to increases in CBF which can serve as an indication for vascular health.

Using blood oxygen level dependent (BOLD) MRI as a surrogate marker for vasodilatory-induced changes in cerebral blood flow (CBF), it

* Corresponding author. Department of Surgery, Queen's University, Room 232, 18 Stuart St., Kingston, ON K7L 3N6, Canada.
E-mail addresses: a.champagne@queensu.ca (A.A. Champagne), a.bhogal@umcutrecht.nl (A.A. Bhogal), nc68@queensu.ca (N.S. Coverdale), clarisse.mark@mail.mcgill.ca (C.I. Mark), blairt@kgh.on.ca (D.J. Cook).
[1] Centre for Neuroscience Studies, Room 260, Queen's University, Kingston ON K7L 3N6.
[2] Department of Radiology, University Medical Center Utrecht, Kamernummer Q024301, Huispostnummer E01132, Postbus 85500, 3508 GA, Utrecht, The Netherlands.
[3] Centre for Neuroscience Studies, Room 233, Queen's University, Kingston ON K7L 3N6.

https://doi.org/10.1016/j.neuroimage.2017.11.044
Received 9 August 2017; Accepted 20 November 2017
Available online 5 December 2017

becomes possible to relate vascular properties to changes in BOLD image contrast. During hypercapnia, it is assumed that changes in venous cerebral volume (CBV_V) occur concurrently with increases in CBF, as highlighted by the Davis model (Chen and Pike, 2009; Davis et al., 1998), and the Grubb's constant (Grubb et al., 1974). As CBF increases, under isometabolic conditions, the concentration of venous deoxygenated hemoglobin ($[dHb_v]$) is reduced, which leads to an increase in blood T_2*, and a concomitant increase in BOLD signal intensity (Ogawa et al., 1990). In traditional CVR mapping, the BOLD signal from the grey matter (GM), or whole brain (Sobczyk et al., 2015), is first time-aligned with the measured end tidal partial pressure of carbon dioxide ($P_{ET}CO_2$). Based on this alignment, the ratio between BOLD signal change to the change in $P_{ET}CO_2$ can be used to determine a voxel-wise map of CVR. In voxels where vessels respond quickly to the vascular stimuli (i.e. mainly in the GM), the BOLD response will be in step with changes in the magnitude of the stimulus. In regions where the CVR response is slow due to vascular impairments, or blood flow distribution effects (Bhogal et al., 2015), delays between changes in vascular stimuli and the measured BOLD signal may become apparent. In general, however, P_aCO_2 modulated changes in the BOLD signal reflect local cerebrovascular properties.

The BOLD contrast mechanism can also be used to examine CBF independent of changes in vascular tone when combined with non-vasoactive hyperoxic breathing challenges. Under healthy baseline conditions arterial hemoglobin is typically fully saturated with O_2 (~98%) and increases from baseline in the arterial partial pressure of oxygen (P_aO_2) leads to increased plasma-dissolved O_2. As blood passes through the capillary networks of the brain, an increased fraction of metabolic demand in the tissues is met via passive diffusion of plasma O_2. Since less O_2 is extracted from hemoglobin, $[dHb_V]$ is reduced, which leads to a lengthening of blood T_2*. This causes a BOLD signal effect similar to that described above for CO_2. However, oxygen-mediated BOLD responses are considered to be uncoupled from CVR, assuming limited vasoconstriction (Mark and Pike, 2012) and a minor reduction in CBF, and thus, CBV_V (D. P. Bulte et al., 2007a, b; Xu et al., 2012). Using this model, hyperoxic changes in BOLD signal can be used to reflect the arrival of blood containing increased O_2 dissolved in plasma, making O_2-rich plasma an endogenous contrast agent for estimation of baseline CBV_V (Blockley et al., 2013; Liu et al., 2017).

The current line of reasoning regarding BOLD-CVR mechanistics assumes that a global vasoactive stimulus mainly elucidates phenomena relating to vascular functioning. This thinking overlooks the possibility that intrinsic blood flow redistribution, the speed of the vascular response to hypercapnia, and response lag related to blood-arrival time are convolved to determine the temporal BOLD-CVR response. The depth of information on vascular responses as measured from the perspective of blood flow delays and flow distribution has facilitated a more comprehensive understanding of the physiology underlying cerebral hemodynamics. Regional BOLD-CVR response delays have been identified in healthy subjects (Blockley et al., 2011; Thomas et al., 2014) where differences have been attributed to cerebrovascular morphology (Bhogal et al., 2015) and the interactions with neighboring tissue compartments (Sobczyk et al., 2014). For example, deep white matter (WM), which is fed primarily from penetrating medullary arteries, experiences delayed arrival times under global hypercapnia since vessels must compete with proximal GM regions which are exposed to the vasoactive stimulus earlier. This phenomenon is in part due to the pial vessel architecture, which inherently delays the bolus arrival times for deeper tissues (Duvernoy, 1981). Greater reductions in peripheral resistance within the GM vascular tree, from hypercapnia, leads to redistribution of blood flow, and an increase in arrival time for downstream deep WM regions. This rationalization regarding the regional heterogeneity of the stimulus response delays recorded in healthy subjects, can be extended to pathological circumstances when CVR delays are particularly apparent due to occlusion (Poublanc et al., 2015), Moyamoya disease (Donahue et al., 2016), atherosclerotic plaque (Donahue et al., 2016), or sickle cell disease (Leung et al., 2016).

A variety of approaches have been employed to examine the temporal dynamics of the BOLD response to hypercapnia. Some of these include frequency-based methods in combination with customized stimulus waveforms to examine phase delays between different regions of the brain (Blockley et al., 2011; Duffin et al., 2015), while others used time-constant based approaches to estimate response delays (Poublanc et al., 2015). Additionally, Donahue et al. (2016) used a data-driven design (Regressor Interpolation at Progressive Time Delays (RIPTiDe)) to model temporal delays in CVR as a function of the global hemodynamic response derived from changes in $P_{ET}CO_2$.

Despite these advances, it remains unclear whether BOLD-CVR response delays during hypercapnia are due to individual variability in cerebrovascular morphology, poor reactivity, or preferential blood flow distribution. In this study, we use the idea that O_2 acts as an endogenous non-vasoactive tracer during hyperoxia to quantify delays that are inherently due to the physiological arrival time of blood in healthy subjects. Combined with information from hypercapnic BOLD-CVR, we introduce a novel method based on the RIPTiDe approach that characterizes temporal delays during hypercapnia, which are corrected using hyperoxia. We purport that this technique can aid in distinguishing between morphological blood flow delays, vascular response speed, and blood flow redistribution between competing vascular territories.

Methods

Subjects and ethical approval

This study was approved by the Queen's University Research Ethics Board and informed consent was obtained from each participant. Participants were recruited from the club and varsity athletics program at Queen's University, as well as from Canadian National teams. Imaging data from 23 healthy volunteers was acquired for this study. Four subjects were removed from the analysis (2 for incomplete datasets, and 2 for poor data quality), resulting in a total of 19 healthy subjects (12 F; 20 ± 2 years).

Experimental protocol

Gas manipulations

End-tidal partial pressures of O_2 ($P_{ET}O_2$) and $P_{ET}CO_2$ were targeted using a computer-controlled gas blending system (RespirAct™, Thornhill Research Inc., Toronto, ON). Subjects were fitted with a facemask, which was sealed using adhesive tape (Tegaderm, 3 M Health Care, St. Paul, MN, US) to prevent any gas leaks. The breathing circuit was then connected to the gas blender for calibration, and subject familiarization with the hypercapnia protocol. From the calibration trial, the subject's baseline parameters were identified. The hypercapnic iso-oxic breathing paradigm consisted of a 2-min baseline period (medical air, 21:79% O_2:N_2), followed by a 2-min hypercapnic challenge where $P_{ET}CO_2$ was targeted to 10 mmHg above the subject's baseline. The administered hypercapnic gas mixture consisted of blend of medical air and CO_2 enriched air (10:21:69% CO_2:O_2:N_2). This was followed by a 2-min recovery period (medical air). $P_{ET}O_2$ was maintained at a baseline value of 110 mmHg throughout. The second breathing paradigm was a hyperoxic iso-capnic challenge during which $P_{ET}CO_2$ was kept constant at the subject's baseline throughout. $P_{ET}O_2$ was targeted at 110 mmHg for 2-min, increased to 410 mmHg for 2-min using a blend of medical air and pure oxygen (100% O_2), and was followed by a recovery period at 110 mmHg $P_{ET}O_2$ for 2-min. Subjects breathed to a metronome at 12 breaths per minute to maintain a constant respiratory rate throughout the breathing paradigms, while end-tidal pressures were sampled continuously by the RespirAct™ (Table 1).

Magnetic resonance imaging data acquisition

All images were acquired on a Siemens 3.0 T Magnetom Tim Trio system using a 32-channel receiver head coil. The imaging protocol

Table 1
Averaged physiological parameters during each breathing paradigm.

	Parameters	Baseline	Stimulus	% Δ	*P-value*
Hypercapnia	GM CBF* (mL/100 g/min)	68.0 ± 5.5	110.1 ± 7.8	65.8 ± 4.2	***P* < 0.001**
	S_aO_2 (%)	98.160 ± 0.005	98.340 ± 0.004	0.19 ± 0.03	***P* < 0.05**
	HB-O_2 (mL_{O2}/dL_{blood})	19.73 ± 0.01	19.77 ± 0.01	0.19 ± 0.03	***P* < 0.05**
	Plasma O_2 (mL_{O2}/dL_{blood})	0.333 ± 0.003	0.345 ± 0.003	3.6 ± 0.5	***P* < 0.05**
	C_aO_2 (%)	20.06 ± 0.01	20.11 ± 0.01	0.24 ± 0.04	***P* < 0.05**
	$P_{ET}CO_2$ (mm Hg)	37 ± 1	45 ± 1	21.0 ± 1.1	***P* < 0.001**
	$P_{ET}O_2$ (mm Hg)	107 ± 1	111 ± 1	3.6 ± 0.5	***P* < 0.05**
Hyperoxia	GM CBF* (mL/100 g/min)	64.9 ± 3.3	65.7 ± 3.7	0.67 ± 3.3	0.82
	S_aO_2 (%)	98.210 ± 0.001	99.950 ± 0.001	1.78 ± 0.07	***P* < 0.001**
	HB-O_2 (mL_{O2}/dL_{blood})	19.74 ± 0.01	20.091 ± 0.001	1.78 ± 0.07	***P* < 0.001**
	Plasma O_2 (mL_{O2}/dL_{blood})	0.337 ± 0.005	1.176 ± 0.045	247.6 ± 9.4	***P* < 0.001**
	C_aO_2 (%)	20.08 ± 0.02	21.27 ± 0.05	5.9 ± 0.2	***P* < 0.001**
	$P_{ET}CO_2$ (mm Hg)	37 ± 1	36 ± 1	−1.24 ± 0.7	0.07
	$P_{ET}O_2$ (mm Hg)	109 ± 1	380 ± 14	248.0 ± 9.1	***P* < 0.001**

C_aO_2 = arterial oxygen content, CBF = cerebral blood flow, GM = grey matter, HB-O_2 = hemoglobin bound oxygen, $P_{ET}CO_2$ = end-tidal pressure of carbon dioxide, $P_{ET}O_2$ = end-tidal pressure of oxygen, S_aO_2 = arterial oxygen saturation, % Δ = percent change from baseline, * = CBF outliers were removed using Tukey's algorithm (factor = 1.5) prior to GM averaging. This table summarizes the physiological characteristics during each gas manipulations for the control subjects (n = 19). Values are in mean ± standard error.

included a T_1-weighted MP-RAGE (magnetization prepared rapid acquisition gradient echo) of the whole brain with the following parameters: TR = 1760 ms, TE = 2.2 ms, TI = 900 ms, voxel size = 1 mm isotropic, FOV = 256 mm.

BOLD and CBF data were simultaneously acquired during hypercapnia and hyperoxia using a dual-echo multi-slice pseudo-continuous arterial spin labeling (pCASL; Alsop et al., 2015) acquisition with the following parameters: TR = 4000 ms, TE1/TE2 = 10/30 ms, field of view = 250 × 250 mm, alpha = 90°, voxel size = 3.9 mm isotropic, post-labeling delay (PLD) = 1000 ms, tagging duration 1.665s (Wu et al., 2007). The acquisition included 25 axial slices with 0.78 mm slice gaps. For quantification of CBF, a tissue equilibrium magnetization map (M_0) was acquired with parameters identical to the pCASL measurements, although TR was longer (15 000 ms), and there was no spin labelling.

Data processing

Estimating CBF and physiological parameters

Cerebral blood flow. CBF was quantified to verify that ΔCBF during hyperoxia was minimal, while an increase was expected during hypercapnia. To reconstruct the perfusion weighted image, a pairwise subtraction of the first-echo ASL image was done between the adjacent tag (selective) and control (nonselective) frames, and subsequently averaged over time. Standard processing steps were applied including motion correction (*FSL* MCFLIRT; Jenkinson et al., 2002), brain extraction (BET), and smoothing (full-width at half maximum (FWHM); 5 mm). The voxel-wise CBF weighted perfusion maps (ml/100 g tissue/min) were calibrated into physiological units and quantified using the single-blood compartment model (Eq. (1)), which assumes that the label remains in the vascular compartment (Wang et al., 2003):

$$CBF = \frac{6000\lambda \cdot \Delta M \cdot e^{delay/T_{1b}}}{2\alpha_{inv} \cdot M_0 \cdot T_{1b} \cdot \left(e^{-w/T_{1b}} - e^{-(\tau+w)/T_{1b}}\right)} \quad (1)$$

In Eq. (1), λ is the blood/tissue water partition coefficient (0.9 ml/g; Herscovitch and Raichle, 1985), ΔM is the average difference in signal between the control and tag states for all perfusion frames, M_0 is the equilibrium magnetization of brain tissue, w is the post labeling delay (1s), τ is the labeling duration (τ = 1.665s), and T_{1b} is the longitudinal relaxation time (T_1) for arterial blood (T_{1b} = 1.650s; Zhang et al., 2012). The post-labeling delay differences between each slice (i) due to the two-dimensional readout were also accounted for using $delay_i$ = w + (s_T)*(i-1), where s_T is the slice time in seconds (0.0538 s). The inversion efficiency (α_{inv}) was set to 0.95 for images obtained during baseline breathing, and throughout hyperoxia (Dai et al., 2008). For images acquired during hypercapnic breathing, α_{inv} was set to 0.85.

During hyperoxic breathing, additional O_2 dissolved in the arterial blood shortens the T_1 relaxation time (Bulte et al., 2007a, b) which can cause brightening of the signal due to faster T_1 recovery. To correct for this, an extension of the model proposed by (Woolrich et al., 2006), in (Germuska et al., 2016) was employed, where the T_1 of blood was allowed to vary throughout the time series. This model assumes a linear relationship between the partial pressure of oxygen (P_aO_2; obtained from the $P_{ET}O_2$ trace) and arterial blood T_{1b}, as the data is fitted using Eq. (2):

$$T_{1b} = b \cdot P_aO_2 + c \quad (2)$$

In Eq. (2), *b* is a fixed value (-5×10^{-4} mm Hg) extrapolated from Ma et al. (2014), and *c* is related to the normoxic T_1 of blood at 3 T using $c = 1.725 - b \cdot 110$. The constant 1.725s is taken from the literature (Lu et al., 2004). Altogether these values were used to convert P_aO_2 to T_{1b}, and correct the hyperoxic CBF quantification Eq. (1).

Oxygen saturation and arterial oxygen content. The arterial oxygen saturation (S_aO_2) was estimated using the Severinghaus equation (Eq. (3); Severinghaus, 1979):

$$S_aO_2 = \frac{1}{\left(\frac{23400}{\left(P_{aO_2}\right)^3 + 150\left(P_{aO_2}\right)} + 1\right)}, \quad (3)$$

where P_aO_2 is replaced by the end-tidal O_2 values recorded during the gas manipulation. Once S_aO_2 was estimated, the arterial oxygen (C_aO_2) content was derived using Eq. (4):

$$C_aO_2 = (\varphi \cdot [Hb] \cdot S_aO_2) + (P_aO_2 \cdot \varepsilon), \quad (4)$$

which represents the sum of the oxygen bound to hemoglobin (first term) and the oxygen dissolved in the plasma (second term). In Eq. (4), φ is the species dependent O_2-carying capacity of hemoglobin (1.34 ml O_2/g_{Hb} for humans), ε is the solubility coefficient of oxygen in blood (0.0031 $mL_{O2}/(dL_{blood}$ mm Hg)), and [Hb] is the concentration of hemoglobin in blood ($[Hb]_{normal}$ = 15 g Hb/dL_{blood}; see Appendix A in Bulte et al., 2012).

BOLD preprocessing

The BOLD data was reconstructed using an addition scheme validated by Bhogal et al. (2016) and Posse et al. (1999). Once parsed, the BOLD images were processed using a combination of FSL, and in-house designed Matlab (MATLAB, 2015b, The MathWorks, Inc., Natick, Massachusetts, United States) scripts. Preprocessing steps included motion correction, removal of non-brain tissues using the brain extraction tool, and voxel-wise linear de-trending to correct for any temporal drift from the scanner acquisition. After the first 5 volumes were removed to allow

the signal to reach a steady baseline state, the BOLD data was normalized to reflect the percent change from the averaged baseline signal, and spatially smoothed using a Gaussian kernel of FWHM of 5 mm. Finally, the recorded end-tidal waveforms ($P_{ET}CO_2$ and $P_{ET}O_2$) were interpolated to the BOLD sampling frequency, and temporally aligned to their respective BOLD time course, extracted from the whole brain mask generated during brain extraction. This step synchronizes the overall BOLD signal change in the brain with the end-tidal data, as a way to remove any delays due to inter-subject differences in arrival time from the lungs to the brain vasculature, and other factors like gas transit time from the RespirAct™ to the mouth.

RIPTiDe pipeline

The RIPTiDe method was implemented by (Tong et al., 2011), and others (Donahue et al., 2016; Frederick, 2012), as a way to calculate the voxel-wise temporal cross-correlation between a probed regressor, and the BOLD data, with the objective of estimating peak time lag values of the hemodynamic response. In this study, a modified RIPTiDe method was used to isolate the hemodynamic component from the BOLD data as a response to the breathing paradigms (Fig. 1), and estimate temporal delays in response to hypercapnic and hyperoxic stimuli.

First, the time courses from each GM voxel were extracted using the subject's GM mask (from T_1 segmentation) transformed non-linearly into native space (Fig. 1A). The refinement steps of the regressing probe were limited to GM voxels due to their higher signal to noise ratio (SNR). This improved the modelling of the hemodynamic response. In the first pass, each extracted GM voxel time series was cross-correlated with the probe regressor (the measured $P_{ET}CO_2$ trace; Fig. 1B). The temporal lags were extracted from the cross-correlation function within a lag range of −5 to 90 s. A univariate Gaussian fit was then applied to the cross-correlation matrix to derive the temporal lag (seconds) and the maximum correlation coefficient (R) for each voxel (Fig. 1C). The peak correlation between the probe and the voxel's BOLD time series occurs at the time lag where both signals are optimally synchronized, which is dependent on the time point when the stimulus passes through the vasculature.

Time series with a correlation coefficient above 0.3, and a time delay magnitude between 0 and 5 s, were extracted (Fig. 1D), since these data best represented the expected physiological response to the stimulus assuming fast reacting healthy vasculature, with low delay indicating limited blood flow distribution effects. These time series were shifted and re-aligned based on their temporal lag, so that the common hemodynamic pattern was in phase. A weighted principal component analysis (PCA) was then used to identify the time course explaining the highest shared variance (Fig. 1E), and thus closely characterized the global hemodynamic response to the stimulus, as described in (Donahue et al., 2016). PCA parameters were set so that a minimum of 80% shared variance was represented by the newly refined regressor (or 3 components minimum). This cycle was repeated until the mean-squared error (MSE) between the probe from the previous round, and the new probe, was less than 0.0005, signifying convergence.

In the last steps of the RIPTiDe method (Fig. 1F–H), the refined regressor was cross-correlated with each voxel's time series contained within a whole-brain mask. The final correlation matrix was fitted using a Gaussian function to estimate maximum correlation and time to peak (TTP) maps. As described in Donahue et al. (2016), the TTP map provides a distribution of the temporal delays in CBF increase, in response to the vasoactive gas challenge. Because the probe is refined using the gas block diagram, and the blood oxygenation waveforms, it models the hemodynamic response more accurately and accounts for physiological noise in the signal. This method improves the final voxel-wise correlation. While the TTP map can be used to compare the hemodynamic latency, the squared correlation map (R^2) reflects the proportion of change in BOLD signal that is modulated by changes in blood CO_2 or O_2 content.

As previously highlighted, delayed arrival time in deeper WM regions, due to blood flow redistribution, may artificially decrease the estimated local vascular reactivity using current CVR mapping. To correct for this, hypercapnic TTP maps were normalized by doing a voxel-wise subtraction using the reference hyperoxic TTP map, after co-registering both into standard space (see below), and setting negative lags values (ranging from −5 to 0 s) to 0. The resultant image from this subtraction is referred to as the calibrated TTP map from here on. This method allowed the blood arrival time to be weighted by the underlying morphology of the vasculature, as step hyperoxic hemodynamic latencies are independent of the vasoactive reserves (under the assumption that CBF is kept relatively constant throughout the hyperoxic gas paradigm; see Table 1 and Fig. 3).

Correcting cerebrovascular reactivity using hypercapnia delays

As previously pointed out, temporal delays in the cerebrovascular response to hypercapnia can result in underestimation of regional CVR,

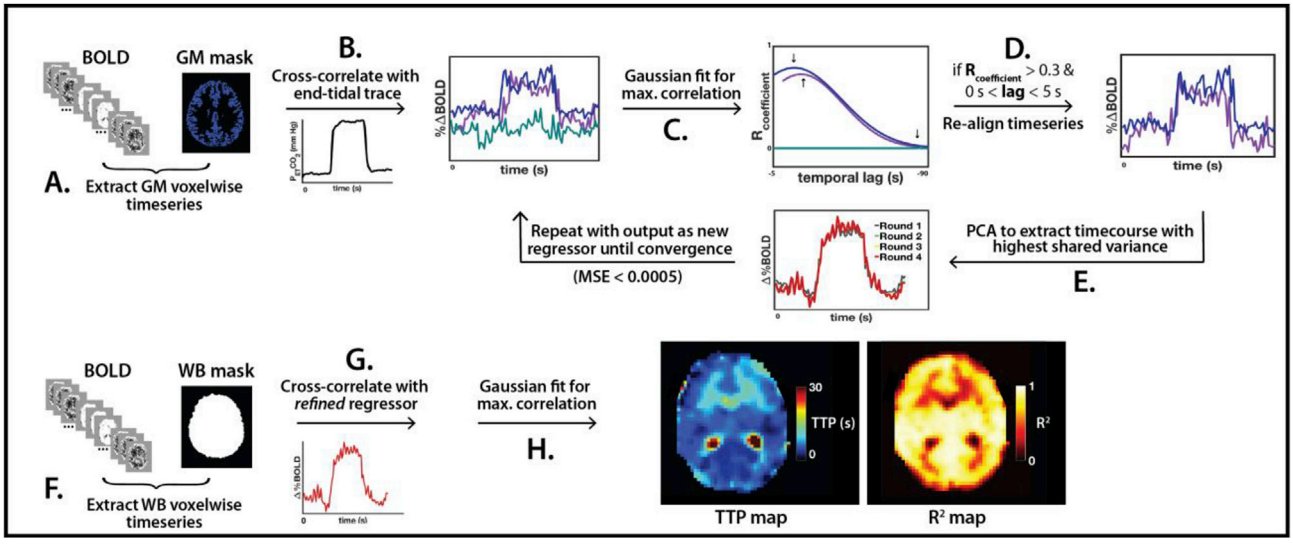

Fig. 1. The RIPTiDe processing pipeline. (**A-E)** The refinement steps used to estimate the probe regressor time course explaining the highest shared variance across voxels. In this illustration, three time series are used as an example of the filtering step prior to re-alignment (blue = high R^2, short lag = passed; purple = high R^2, minor lag = passed; turquoise = low R^2, large lag = not passed). (**F-H)** Deriving the peak time delay (s) and the squared maximal correlation coefficient (R^2) at each location. BOLD = blood oxygen level dependent, GM = grey matter, MSE = mean-squared error, PCA = principal component analysis, $P_{ET}CO_2$ = end tidal carbon dioxide, RIPTiDe = Regressor Interpolation at Progressive Time Delays, TTP = time to peak (s).

which is an important limitation to overcome for clinical use of reactivity mapping. In order to highlight this process, we used the TTP map from hypercapnia to generate a new corrected CVR map ($CVR_{corrected}$), in each individual. First, a traditional CVR map ($CVR_{traditional}$) was generated using a linear voxel-wise least-square fit of the original (non-corrected) BOLD response to the $P_{ET}CO_2$ waveform. This method maps CVR at each voxel in terms of percent change in BOLD signal per unit of change in $P_{ET}CO_2$ (%ΔBOLD/mmHg).

To generate the $CVR_{corrected}$ maps, BOLD timeseries at each voxel were time-shifted using the co-localized hypercapnia TTP magnitude (Fig. 2A–B), in order to improve the synchronization between the signal change and $P_{ET}CO_2$ (Fig. 2C–F). The new slope between the time-shifted signal change and the end-tidal waveform improves the estimation of CVR by providing an estimate of the vasodilatory capacity that is corrected for temporal delays due to the vascular morphology, or possible blood flow redistribution across tissues.

Spatial normalization and masking

Individually processed CVR maps and TTP maps from hypercapnia and hyperoxia were co-registered to their high-resolution T_1 structural image. Structural images were then spatially normalized to the Montreal Neurological Institute (MNI) standard template (resolution: 2-mm isotropic voxels) using linear rigid body transformations (*FLIRT*; Jenkinson et al., 2002b; Jenkinson and Smith, 2001), and non-linear warp-fields (*FNIRT*; Andersson et al., 2007). The final deformation parameters were concatenated to warp the functional data series and the perfusion maps into MNI standard space for regional analysis across subjects.

In order to differentiate between late arrival time, poor reactivity and preferential flow, the group averaged calibrated TTP map was weighted and labelled using the traditional CVR (%BOLD/mmHg) and hypercapnia TTP maps. CVR was split into three categories (low, moderate and high), which were determined using the following ranges: low ($CVR_{traditional} < 0.01$ %BOLD/mmHg), moderate ($0.01 \leq CVR_{traditional} \leq 0.1$), high ($CVR_{traditional} > 0.1$). Hypercapnia TTP delays were separated into two categories (short and long), using 5 s as the hypercapnia TTP threshold.

Regional analysis of delays and cerebrovascular reactivity

A region of interest (ROI) analysis was performed to examine the distribution of temporal lags and $CVR_{corrected}$ across the brain, and at different tissue depths. GM anatomical ROIs included the frontal, temporal, parietal and occipital lobes, which were defined using the probabilistic MNI brain atlas (Mazziotta et al., 2001). Additionally, GM structures including the caudate, insula, putamen and thalamus were combined to make up the deep GM ROI.

Automatic 3D tissue segmentation of the warped MP-RAGE T_1 in MNI space was done using *FAST* (FSL; Zhang et al., 2001) to separate the GM, WM and cerebrospinal fluid (CSF). To control for anatomical variation across subjects, each GM structure from the atlas was defined by the maximum probability estimate (thresholded at 0) and masked using the individually segmented GM mask excluding voxels with a GM probability lower than 50%. Different tissue depth of the WM were defined using a combination of subtractions and erosions of the subject's segmented WM NIFTI image (Fig. 3).

The resultant GM and WM ROIs were used to perform volumetric weighted averaging of the $CVR_{corrected}$, hypercapnic and hyperoxic TTP, and the calibrated TPP ($hypercapnic_{TTP}$ - $hyperoxic_{TTP}$) maps across subjects. Regional parameters across the GM and WM depth were statistically compared using a repeated measures ANOVA, and Bonferroni correction. GM perfusion and physiological parameters (SaO_2 and CaO_2) between the baseline and stimulus periods, were compared using a paired two tailed Student's T-test. Statistical significance for all comparisons was set at $P < 0.05$.

Results

Comparing physiological parameters between breathing challenges

During hypercapnia, $P_{ET}CO_2$ increased by 21.0 ± 1.1%, which was accompanied by a significant 65.8 ± 4.2% increase in GM CBF (Table 1). The increase in CBF during hypercapnia is also evident from the group averaged perfusion maps (Fig. 4). $P_{ET}O_2$ was maintained (±3.4%) during

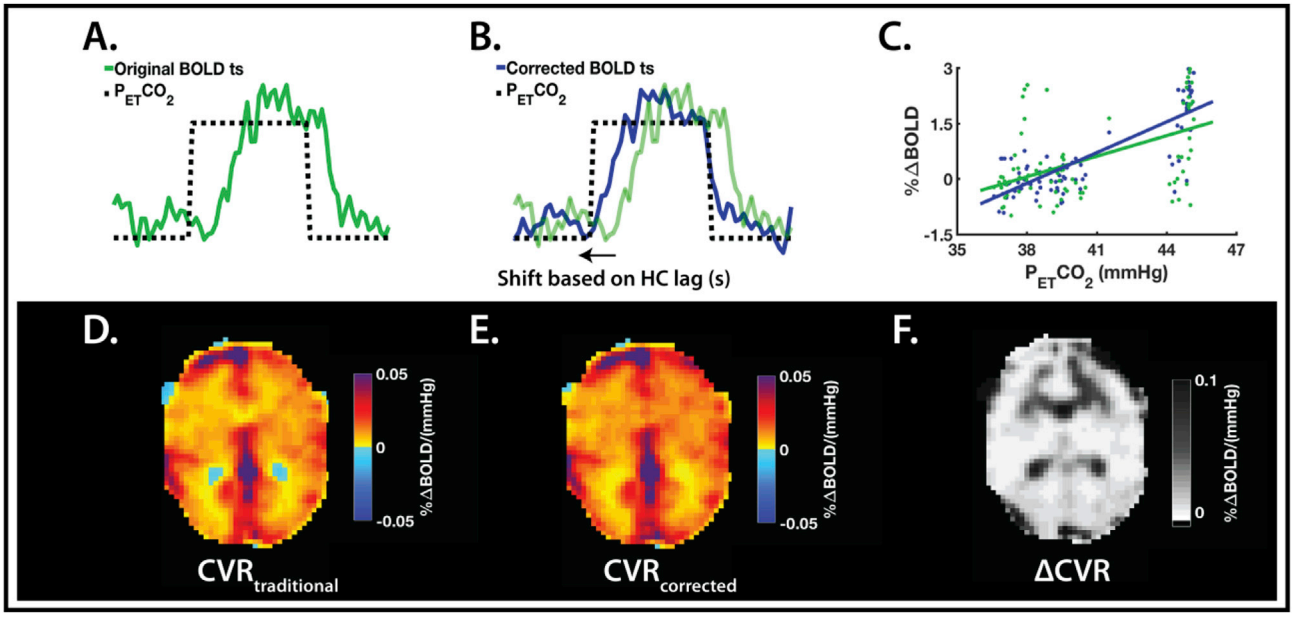

Fig. 2. Voxel-wise cerebrovascular reactivity corrections using the hypercapnic temporal lag. (**A**) A sample BOLD time course delayed by 10 s (green), plotted over the targeted $P_{ET}CO_2$ (10 mmHg above baseline). (**B**) The original BOLD time course (green) temporally shifted by the hypercapnia TTP. (**C**) The least-square regression between both original and corrected BOLD time course, and the actual $P_{ET}CO_2$. CVR (%ΔBOLD/mmHg) is equal to the slope of the regression. (**D**) The traditional CVR map. (**E**) The corrected CVR map for temporal delays. (**F**) A difference map between **E** and **D** to show co-localized similarities with the TTP map shown in Fig. 1H. BOLD = blood oxygen level dependent, CVR = cerebrovascular reactivity, $P_{ET}CO_2$ = end-tidal carbon dioxide, TTP = time to peak (seconds).

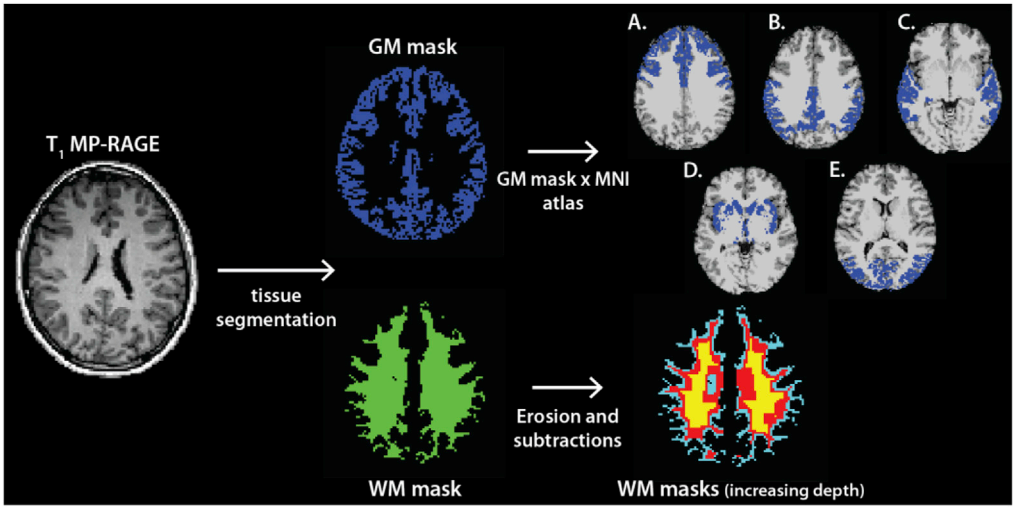

Fig. 3. Subject-specific ROI definitions in standard space. The T_1 MP-RAGE anatomical images were warped to MNI space, and segmented into GM and WM masks using FSL *FAST*. To reduce the likelihood of GM (blue) and WM (green) partial volume overlapping, a probabilistic threshold (GM ≥ 50% probability, WM ≥ 90% probability) was set for voxels in each tissue. GM structures (**A-E**) were defined using the co-localized voxels between the subject's GM probability mask and the MNI atlas (**A.** frontal, **B.** parietal, **C.** temporal, **D.** deep GM (caudate, insula, putamen and thalamus), and **E.** occipital). To evaluate hemodynamic latencies across different WM depth, the individual's WM (green) was eroded three-dimensionally three consecutive times, and subsequently subtracted to define deeper WM masks (cyan, red and yellow). The final GM and WM masks were applied to each map for further analyses. GM = grey matter, MNI = Montréal Neurological Institute, ROI = region of interest, WM = white matter.

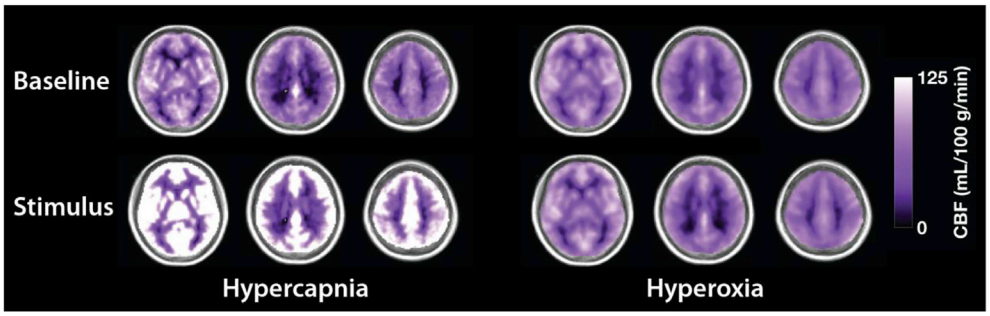

Fig. 4. Group averaged perfusion maps. Baseline (top) and stimulus (bottom) mean CBF weighted maps during each gas manipulation (hypercapnia = left, hyperoxia = right). CBF outliers were removed in each individual prior to averaging using Tukey's algorithm (factor = 1.5). Average maps were smoothed using a 5 mm FWHM filter, and overlaid on top of the group averaged anatomical image. CBF is quantified in mL/100 g/minutes. Note the significant changes in CBF under hypercapnia (Table 1), due to the vasoactive nature of the stimulus. CBF = cerebral blood flow, FWHM = full-width at half maximum.

hypercapnia, which is also reflected by very minor changes in oxygen saturation ($\Delta SaO_2 = 0.19 \pm 0.03\%$) and oxygen arterial content ($\Delta CaO_2 = 0.24 \pm 0.04\%$).

During hyperoxia, on average, $P_{ET}CO_2$ was maintained within ±1.24%, and GM CBF did not change (Table 1, Fig. 4). Plasma O_2 content increased by 247.6 ± 9.4% and this contributed to a 5.9 ± 0.2% increase in arterial oxygen content.

Cerebrovascular reactivity and hemodynamic latencies

Across the GM, the squared maximal correlation coefficient (R^2) was higher during hypercapnia, which is represented by the brighter signal in Fig. 5B, compared to Fig. 5D. Furthermore, CVR correction for temporal delays provided a more accurate estimation of local vascular reactivity, that is independent of regional hemodynamic latencies (Table 2, Fig. 6). Corrected vascular reactivity to hypercapnia was higher in GM regions throughout the brain when compared to WM tissues ($P < 0.05$, Bonferroni corrected; Table 2, Fig. 7A). Additionally, on average between subjects, decreasing $CVR_{corrected}$ values were found as the depth of the WM increased.

Hemodynamic latencies also differed between hypercapnia and hyperoxia (Table 2, Fig. 5C and E, Fig. 7B and C). In all GM and WM regions, except the deep WM, the magnitude of TTP was higher on average during hyperoxia when compared to hypercapnia. The opposite was observed in the deep WM tissue, where the delay times during hypercapnia (8.5 ± 1.6 s) was longer than the deep WM delay during hyperoxia (8.3 ± 1.6 s). Hypercapnic temporal delays also increased as the depth of the WM tissue increased (Table 2, Fig. 7B), although no significant differences in TTP were found across WM tissue depth, or between the cortical GM and the WM (Fig. 7B and C, right).

The physiological estimation of CBF arrival time through hyperoxic delays was used to normalize the hypercapnic TTP maps, and highlight dynamic blood flow distribution across different regions, and tissues depth, of the cerebrovasculature. Averaged calibrated delay map following the voxel-wise subtraction between the hypercapnic and hyperoxic TTP maps in each subject showed that the majority of voxels with a positive calibrated delay time were in the deeper WM (Fig. 5F). Furthermore, although cortical and subcortical GM regions showed distinct differences in hypercapnic and hyperoxic TTP (Fig. 7B–C), the calibrated delay times revealed more homogenous hemodynamic latencies varying around −1.8 ± 1.2 s (Table 2), which were not statistically significant ($P > 0.05$, Bonferroni corrected; Fig. 7D). In contrast, deeper WM layers showed increasingly more positive calibrated delay times, compared to the GM (Fig. 7D), although these differences were not significant.

Discussion

Main findings

The present study is the first to combine hemodynamic delays measured in response to hypercapnia, and hyperoxia, in order to provide insight into the differences in vascular reactivity between cortical regions, and across tissue depths. Using non-vasoactive hyperoxic delays to

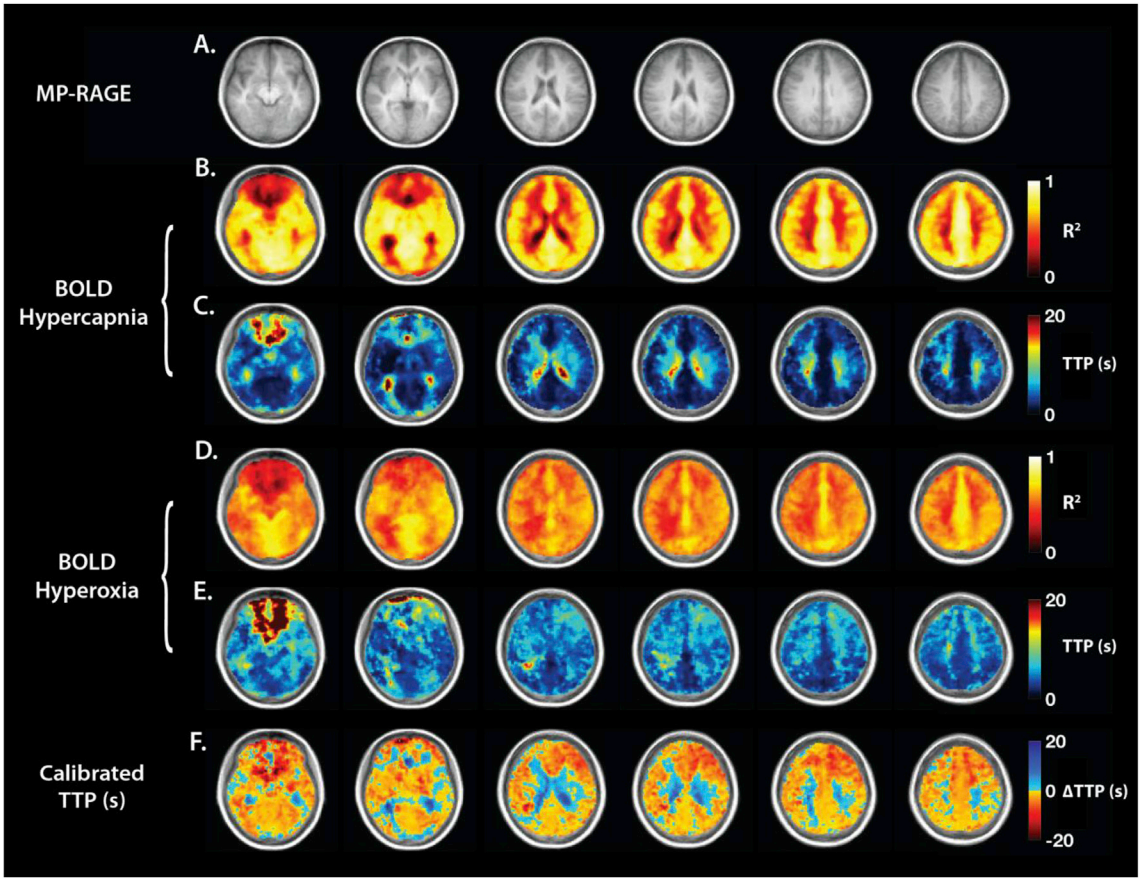

Fig. 5. BOLD normative squared maximal correlation and time to peak maps for healthy controls. (A) The group averaged anatomical image in MNI standard space. **(B-C)** The averaged R^2 (B) and TPP (C) maps during BOLD hypercapnia. **(D-E)** The averaged R^2 (D) and TPP (E) maps during BOLD hyperoxia. **(F)** The group-averaged calibrated TTP map, which is the result of a voxel-wise subtraction between the BOLD hypercapnic and hyperoxic TTP maps. Blue represents voxels where the delay time was longer under hypercapnia (positive calibrated TTP magnitude). Yellow/red represents voxels where the delay time was longer under hyperoxia (negative calibrated TTP magnitude). All maps in **B-F** were smoothed using a 5 mm FWHM Gaussian filter, and overlaid on top of the group averaged anatomical image. BOLD = blood oxygen level dependent, FWHM = full-width at half maximum, MNI = Montréal Neurological Institute, R = maximal correlation coefficient, TTP = time to peak (seconds).

Table 2
Group averaged regional cerebrovascular reactivity and hemodynamic delays.

ROI	CVR (%ΔBOLD/mmHg)		TTP (s)		Calibrated TTP (s)
	Traditional	Corrected	Hypercapnia	Hyperoxia	
Frontal	0.18 ± 0.02	0.21 ± 0.02	8.4 ± 1.1	10.4 ± 1.4	−2.1 ± 1.4
Parietal	0.20 ± 0.01	0.21 ± 0.01	4.0 ± 0.7	5.8 ± 1.1	−1.5 ± 1.1
Temporal	0.18 ± 0.01	0.21 ± 0.01	7.5 ± 0.9	9.4 ± 1.1	−1.9 ± 1.5
Occipital	0.25 ± 0.01	0.28 ± 0.01	3.7 ± 0.5	6.3 ± 1.0	−2.3 ± 0.8
Deep GM$^+$	0.12 ± 0.01	0.14 ± 0.01	6.0 ± 0.8	7.4 ± 1.7	−1.1 ± 1.6
GM cortical	0.18 ± 0.01	0.21 ± 0.01	6.3 ± 0.7	8.2 ± 1.1	−1.8 ± 1.2
WM total	0.09 ± 0.01	0.11 ± 0.01	7.8 ± 1.3	8.4 ± 1.3	−0.3 ± 1.7
WM outer	0.11 ± 0.01	0.13 ± 0.01	7.0 ± 1.0	8.2 ± 1.2	−1.1 ± 1.5
WM inner	0.08 ± 0.01	0.09 ± 0.01	8.0 ± 1.3	8.5 ± 1.4	−0.2 ± 1.8
WM deep	0.06 ± 0.01	0.08 ± 0.01	8.5 ± 1.6	8.3 ± 1.6	1.0 ± 2.3

GM = grey matter, R = correlation coefficient, ROI = region of interest, TTP = time to peak (seconds), WM = white matter.+= deep grey matter region includes the caudate, insula, putamen and thalamus. Values are in mean ± standard error.

normalize CVR lag times, we were able to distinguish between hemodynamic latencies arising due to late stimulus arrival time (morphological delay), or changes in preferential blood flow determined at vascular bifurcations feeding tissues at increasing cerebral depth.

One of the main findings in this study is that different layers of the WM (i.e. the outer and inner WM) may be more susceptible to transient redistribution of flow under vasoactive hypercapnia, which can introduce a delay ranging between 1 and 3 s in healthy subjects. This is likely due to the fact that the WM must compete with more proximal and highly reactive GM vessels for flow (Bhogal et al., 2015; Faraci and Heistad, 1990). In comparison, BOLD signal changes in deeper WM tissues may have longer delay times during hypercapnia due to poor reactivity. Results from this study showed that response lags (both hypercapnia and calibrated TTP) were longer in the WM, compared to the GM, which is consistent with previous work (Thomas et al., 2014). Additionally, relative response time to changes in $P_{ET}CO_2$, once calibrated for arrival time using hyperoxia, did not differ, on average, between GM cortical and subcortical regions (Fig. 7D). This is contrary to previously reported

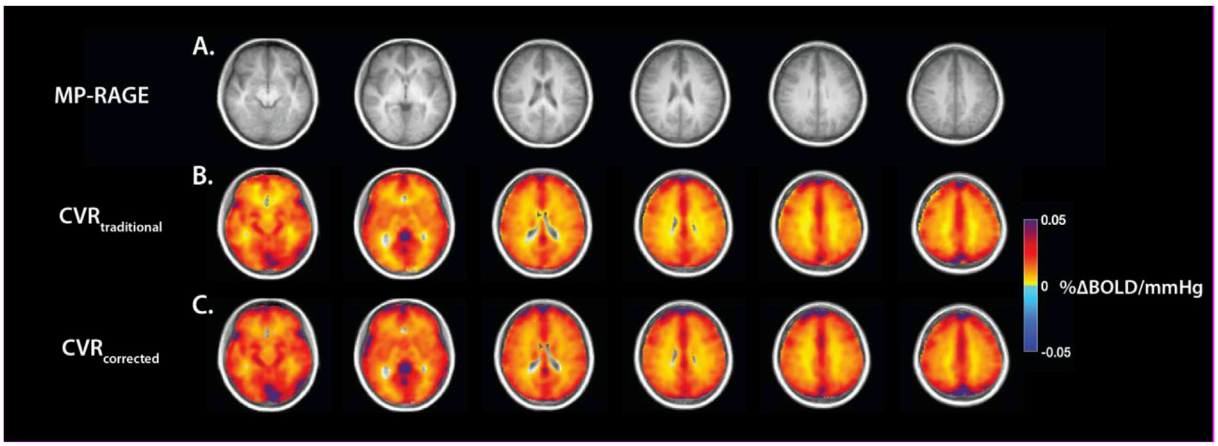

Fig. 6. Group averaged cerebrovascular reactivity maps corrected for temporal delays. (A) The anatomical reference images. **(B)** The group averaged traditional CVR maps. **(C)** The averaged corrected CVR maps adjusted for the hypercapnic delay, as shown in Fig. 5C. Signal change from the ventricles was masked out in **B** and **C**, and images were smoothed using a 5 mm FWHM filter. CVR is expressed in percent BOLD change per mmHg of CO_2 (%ΔBOLD/mmHg). BOLD = blood oxygen level dependent, CVR = cerebrovascular reactivity, CO_2 = carbon dioxide.

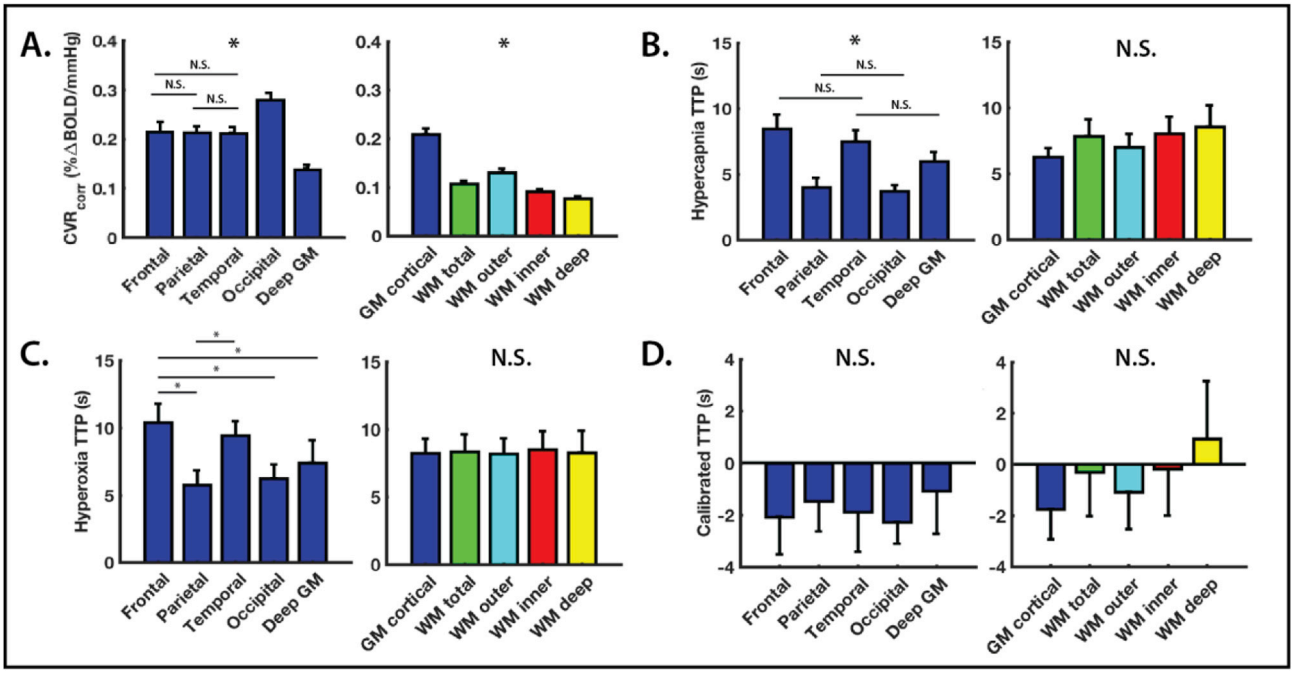

Fig. 7. Statistical results from the regional analysis of vascular reactivity and delays. Results from the repeated measures ANOVA on parameter maps (**(A)** Corrected CVR (%ΔBOLD/mmHg) **(B)** Hypercapnia TTP, **(C)** Hyperoxia TTP, **(D)** Calibrated TTP) between different GM structures (left) and across tissue depth (right). The asterisks (*) highlight significant differences ($P < 0.05$; Bonferroni corrected). Note that the single asterisks in **(A)** and **(B)** show significant differences across all regions except the ones labelled (N.S. = not significant). Bars and error bars represent the mean and standard error, respectively. BOLD = blood oxygen level dependent, CVR_{corr} = corrected cerebrovascular reactivity, GM = grey matter, ROI = region of interest, TTP = time to peak, WM = white matter.

findings (Blockley et al., 2011), although hypercapnic delay times in Blockley's paper were normalized to the entire GM delay, and not calibrated for the hyperoxic bolus arrival time. Significant regional differences in GM CVR corrected for hypercapnia temporal lags (Table 2, Fig. 7A), despite homogeneity in calibrated TTP between cortical and subcortical GM regions (Table 2, Fig. 7D), suggests that differences may be due in part to factors other than arrival time of the CO_2 stimulus. These factors may include true variations in regional vascular reactivity (arteriolar vasodilatory response to hypercapnia), or the effect of additional saturated venous blood from large draining veins (i.e. superior sagittal sinus) on changes in the BOLD signal (i.e. the occipital lobe; Kennerley et al., 2010). This complex relationship may also be altered in clinical populations where CVR is impaired, which emphasizes the need for calibrated TTP maps.

Interpreting the calibrated TTP maps

The RIPTiDE method improved on traditional CVR mapping by creating a regressor that was defined using PCA, and accounted for the highest shared variance within an individual's vascular response. Using a combination of the traditional CVR map (not corrected for delays), and the hypercapnic TTP map, we can distinguish between voxels with poor reactivity (low $CVR_{traditional}$ and long TTP), and voxels with normal reactivity, that are simply delayed (moderate-high $CVR_{traditional}$ and long TTP). The calibrated TTP map used in this method provided a novel estimate of stimulus arrival during hypercapnia, since O_2 was used as an

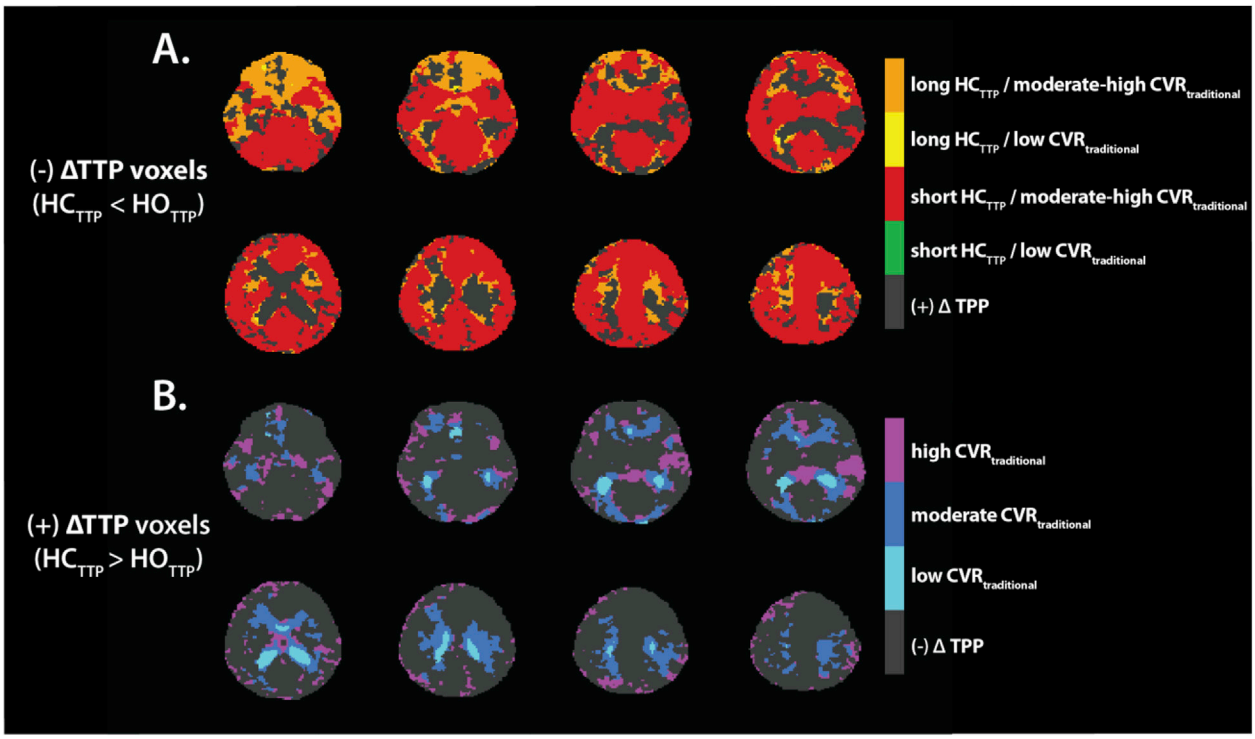

Fig. 8. Voxelwise weighted averaged calibrated time delay maps. Voxels from Fig. 5F were weighted and labelled using the group averaged traditional CVR and hypercapnia TTP maps from Figs. 5B and 6B. **(A)** Highlights only voxels with a negative calibrated TTP, which signifies that the delay time under hypercapnia was shorter than hyperoxia. Green and red voxels represent regions with short hypercapnia delay (≤5 s) and low (green; < 0.01 %ΔBOLD/mmHg) or moderate to high (red; ≥ 0.01 %ΔBOLD/mmHg) $CVR_{traditional}$. Yellow and orange voxels highlight regions where the hypercapnia time delay was long (>5 s). Once normalized using the step hyperoxia TTP, yellow voxels show regions with low (<0.01 %ΔBOLD/mmHg) reactivity despite behind delayed. Orange voxels on the other hand have moderate-high (≥0.01 %ΔBOLD/mmHg) vascular reactivity, but are likely delayed due to the late blood arrival time. **(B)** This map only shows voxels with a positive calibrated TTP (s), which signifies that the delay time under hypercapnia was longer than in hyperoxia. Dark blue and purple voxels (moderate and high CVR) likely represent regions where there is preferential redistribution of blood flow under hypercapnia. Cyan voxels likely represent regions where the HC delay times are long simply due to poor reactivity. CVR = cerebrovascular reactivity, HC = hypercapnia, HO = hyperoxia, TTP = time to peak (seconds).

endogenous contrast agent to model the vasculature, independently of the vascular reactivity. To further illustrate how the maps should be interpreted when subtracting hyperoxic TTP from hypercapnic TTP, voxels were assigned a positive or negative value, dependent on the relative difference in delay times during each gas manipulation (Fig. 8).

Voxels with a negative calibrated TTP

Negative voxels (Fig. 8A) represent regions where the hypercapnic TTP was shorter than hyperoxic TTP. In these regions, blood flow was accelerated during hypercapnia, as expected (Donahue et al., 2014), which reduced the arrival time of the vasoactive stimulus. Red voxels, which constitute most of the GM, have a typical CVR response, as they have a short hypercapnic TTP value (≤5 s), and a moderate to high CVR amplitude ($CVR_{traditional}$ ≥ 0.01 %ΔBOLD/mmHg). These voxels (along with Fig. 7D and Table 2) provide additional evidence that GM reacts faster than WM during step hypercapnia, and with greater magnitude (Fig. 7A), which is consistent with the literature on regional CVR (Bhogal et al., 2015; Blockley et al., 2011; Donahue et al., 2016; Duffin et al., 2015; Poublanc et al., 2015), and temporal differences in blood flow (Rostrup et al., 2000). On the other hand, yellow and orange voxels were found to have longer hypercapnia response lags (>5 s), which would inherently reduce the magnitude of CVR using traditional methods. This is because the delayed BOLD signal may still be increasing beyond the plateau phase of the gas challenge, which would decrease the ratio between the voxel's response and changes in mmHg of CO_2. Following hypercapnic delay calibration, in combination with the $CVR_{traditional}$ map, we speculate that long hypercapnic lags in yellow voxels ($CVR_{traditional}$ ≤ 0.01 %ΔBOLD/mmHg) were due to a blood volume effect. The low GM CVR magnitude suggests that such voxels may contain more parenchymal or CSF contributions, rather than blood (and thus a lower total change in [dHb_v] during hypercapnia), reducing the CBF-induced change in BOLD signal. In comparison, orange voxels have moderate to high CVR ($CVR_{traditional}$ > 0.01 %ΔBOLD/mmHg), and thus, are likely delayed due to the vascular morphology, which increases blood arrival time to the vascular beds of the tissue, and therefore, increases the time required extravascular CO_2 to accumulate. This is an important distinction that was not possible using the non-calibrated hypercapnic TTP and traditional CVR maps independently, highlighting the importance of the proposed method. Regions with lower CVR due to delayed bolus arrival time may be mistakenly labelled as impaired using current BOLD CVR/delay mapping techniques.

Voxels with a positive calibrated TTP

Colored voxels (Fig. 8B) have a positive calibrated TTP, which indicates that the hypercapnic lag time was longer than during hyperoxia. Here, the likely sources for longer delay times during hypercapnia could be poor vascular reactivity (cyan), or dynamic blood flow redistribution (blue/purple) among neighboring regions with greater vasodilatory reserves. Following an increase in P_aCO_2, dense GM arterioles can decrease their peripheral resistance earlier since, due to earlier blood arrival time, they are exposed to the vasoactive stimulus first (Duvernoy et al., 1981). This effect is propagated along the vascular tree, which delays the bolus arrival time of hypercapnic blood to deeper WM tissues, competing for a limited flow (Bhogal et al., 2015; Sobczyk et al., 2014), and obscure the timing of CVR measurements. It is imperative to note that this effect is absent under hyperoxia. Because O_2 is non-vasoactive, this preferential flow phenomenon is not possible, and it can be concluded that hyperoxic delays are mainly dependent on the morphology of the

cerebrovasculature, and the local mean transit time for blood with greater plasma O_2 saturation to pass from the arterial to the venous circulation. As the calibrated TTP increases with WM depth (Fig. 7D), we can combine information from the traditional CVR map (Table 2, Fig. 6B) to differentiate whether the longer delays during hypercapnia occur due to low vascular reactivity (Fig. 8B cyan) or blood flow redistribution (Fig. 8B blue/purple). The preferential flow hypothesis is based on the findings that longer response lags in parts of the WM are not due to a longer transit time, since hyperoxia TTP is similar across tissue depth. Furthermore, CVR in these voxels is moderate to high ($CVR_{traditional} > 0.01$ %ΔBOLD/mmHg). Therefore, the WM delayed response in CVR must be dependent on mechanisms by which the hypercapnic blood flow is temporally redirected, in response to the stimuli, at branching points along the vascular network between GM and WM compartments (Bhogal et al., 2015). Additional voxels with positive calibrated TTP sparsed around the edges of the brain are likely attributable to partial volume effects due to CSF, or registration artifacts across healthy controls.

Limitations

This method employed the RIPTiDe pipeline to estimate CVR, and differences in temporal delays between hypercapnia and hyperoxia. RIPTiDe quantifies time lags based on a fit between the BOLD response signal and the probed regressor. Even though the regressor is refined using RIPTiDe, the quality of this synchronization is limited in hyperoxia given the lower SNR in the data (Fig. 5D), and smaller changes in BOLD during the step stimulus. The BOLD contrast to noise of the hyperoxia response could be enhanced by acquiring additional blocks of hyperoxic measurements, as seen in calibrated fMRI studies (Bulte et al., 2012; Germuska et al., 2016). This would lead to a reduction in noise contributions and therefore, better correlations and more accurate delay estimations. Under step hypercapnia, the partial volume effects of CSF (not reactive) reduces the BOLD signal change, and thus lowers the R^2 coefficient in the ventricles and towards the top of the brain. Additionally, lower SNR in the WM may also limit estimation of both temporal delays and CVR, especially towards deeper tissue layers. Moving to ultra-high (7 T+) field strength could yield similar benefits.

Temporal delays in vascular reactivity were calibrated with an indirect measure of arrival time, estimated using O_2 as an endogenous tracer. This is based on the assumption that O_2 has limited vasoconstrictive effects, although this remains a point of debate (Bulte et al., 2007a, b; Floyd et al., 2003; Tajima et al., 2014). The use of simultaneous peripheral NIRS (Near Infrared Spectroscopy) to characterize vascular contributions to the BOLD signal delays would improve this method by providing measures of cerebral blood volume changes, although this presents additional methodological limitations. These phenomena may be more complex in clinical populations where systematic prolonged arrival delays will limit the pCASL signal (based on the length of the PLD), and thus results in underestimation of the BOLD and CBF data.

This method cannot differentiate whether regions have low CVR due to their resting vascular tone being closer to their maximal dilated state, impaired arteriolar vasodilatory capacity (inability to respond), or low regional arteriolar density (Moody et al., 1990). In the future, data from a normoxic hypercapnic ramp, where $P_{ET}CO_2$ is progressively increased to a maximum target (i.e. 15–20 mm Hg above baseline), could be used to provide additional information about the vessels' vasodilatory reserve (Bhogal et al., 2014). Combined with the calibrated TTP map from the hypercapnic step, which is ideal to model speed of response, this should give a complete picture of the cerebrovascular physiology, and potential CVR impairments.

While the RespirAct™ provided a consistent delivery system to target different end-tidal pressures, its sensitivity in indirectly estimating physiological parameters such as changes in arterial oxygen content and saturation is limited. More accurate instruments such as pulse oximeters will improve those readings. Furthermore, other possible delivery systems could be used to implement this calibrated analysis, provided that normocapnia and normoxia can be properly maintained during each gas manipulations.

Conclusion

We expand on previously introduced techniques to highlight transient differences in cerebrovascular reactivity between cortical GM and WM tissues at varying depth. By combining hypercapnic and hyperoxic gas mixtures, this novel design provided additional information about bolus arrival time and reactivity timing differences, which helped differentiate possible causes for longer temporal delays during hypercapnia. Calibrated TPP maps are an important addition to providing insights about the cerebrovascular physiology, and better distinguish between areas with impaired vascular reactivity, and others with healthy CVR, that may be delayed due to blood flow redistribution, a direct consequence of the global vasoactive hypercapnic stimulus.

Funding

This work was supported by the Canadian Institutes of Health Research (CIHR) (CHRP 307896) and the Natural Sciences and Engineering Research Council (NSERC) through a Collaborative Health Research Project Grant (#315705).

List of Abbreviations

Abbreviation	Meaning
BET	brain extraction tool
BOLD	blood oxygen dependent level
C_aO_2	arterial oxygen content
CBF	cerebral blood flow
CBV_V	venous cerebral blood volume
CO_2	carbon dioxide
CSF	cerebrospinal fluid
CVR	cerebrovascular reactivity
dHb_v	concentration of venous deoxygenated hemoglobin
FWHM	full-width at half maximum
GM	grey matter
HB-O_2	hemoglobin bound oxygen
M_0	magnetization map
MSE	mean-squared error
MNI	montréal Neurological Institute
MP-RAGE	magnetization prepared rapid acquisition gradient echo
MRI	magnetic resonance imaging
O_2	oxygen
P_aCO_2	arterial partial pressure of carbon dioxide
P_aO_2	arterial partial pressure of oxygen
PCA	principal component analysis
pCASL	pseudo-continuous arterial spin labeling
PLD	post-labeling delay
$P_{ET}CO_2$	end-tidal carbon dioxide
$P_{ET}O_2$	end-tidal oxygen
R	maximum correlation coefficient
RIPTiDe	regressor interpolation at progressive time delays
ROI	region of interest
S_aO_2	arterial oxygen saturation
SNR	signal-to-noise ratio
TTP	time to peak
WM	white matter

Acknowledgements

We would like to thank Don Brien for helping with data collection. The authors would also like thank Dr. Blaise Frederick (McLean Imaging Center, MA, USA) for his willingness to share knowledge about the RIPTiDe method, Dr. Patrick Stroman for his help with the PCA methodology (Centre for Neuroscience studies, Queen's University, Kingston, ON) and Dr. Jeroen C.W. Siero (University Medical Center Utrecht, The Netherlands) for his insight regarding this manuscript.

References

Alsop, D.C., Detre, J.A., Golay, X., Günther, M., Hendrikse, J., Hernandez-Garcia, L., Lu, H., Macintosh, B.J., Parkes, L.M., Smits, M., Van Osch, M.J.P., Wang, D.J.J., Wong, E.C., Zaharchuk, G., 2015. Recommended implementation of arterial spin-labeled Perfusion mri for clinical applications: a consensus of the ISMRM Perfusion Study group and the European consortium for ASL in dementia. Magn. Reson. Med. 73, 102–116. https://doi.org/10.1002/mrm.25197.

Andersson, J.L.R., Jenkinson, M., Smith, S., 2007. Non-linear registration aka spatial normalisation FMRIB technial report TR07JA2. Pract 22.

Bhogal, A.A., Philippens, M.E.P., Siero, J.C.W., Fisher, J.A., Petersen, E.T., Luijten, P.R., Hoogduin, H., 2015. Examining the regional and cerebral depth-dependent BOLD cerebrovascular reactivity response at 7T. Neuroimage 114, 239–248. https://doi.org/10.1016/j.neuroimage.2015.04.014.

Bhogal, A.A., Siero, J.C.W., Fisher, J.A., Froeling, M., Luijten, P., Philippens, M., Hoogduin, H., 2014. Investigating the non-linearity of the BOLD cerebrovascular reactivity response to targeted hypo/hypercapnia at 7T. Neuroimage 98, 296–305. https://doi.org/10.1016/j.neuroimage.2014.05.006.

Bhogal, A.A., Vis, J.B., De, Siero, J.C.W., Petersen, E.T., Luijten, P.R., Hendrikse, J., Philippens, M.E.P., Hoogduin, H., 2016. NeuroImage the BOLD cerebrovascular reactivity response to progressive hypercapnia in young and elderly. Neuroimage 139, 94–102. https://doi.org/10.1016/j.neuroimage.2016.06.010.

Blockley, N.P., Driver, I.D., Francis, S.T., Fisher, J.A., Gowland, P.A., 2011. An improved method for acquiring cerebrovascular reactivity maps. Magn. Reson. Med. 65, 1278–1286. https://doi.org/10.1002/mrm.22719.

Blockley, N.P., Griffeth, V.E.M., Germuska, M.A., Bulte, D.P., Buxton, R.B., 2013. An analysis of the use of hyperoxia for measuring venous cerebral blood volume: comparison of the existing method with a new analysis approach. Neuroimage 72, 33–40. https://doi.org/10.1016/j.neuroimage.2013.01.039.

Brian, J.E., 1999. Carbon dioxide and the cerebral circulation. Anesthesiology 88, 1365.

Bulte, D., Chiarelli, P., Wise, R.G., Jezzard, P., 2007a. Measurement of cerebral blood volume in humans using hyperoxic MRI contrast. J. Magn. Reson. Imaging 26, 894–899. https://doi.org/10.1002/jmri.21096.

Bulte, D.P., Chiarelli, P. a, Wise, R.G., Jezzard, P., 2007b. Cerebral perfusion response to hyperoxia. J. Cereb. Blood Flow. Metab. 27, 69–75. https://doi.org/10.1038/sj.jcbfm.9600319.

Bulte, D.P., Kelly, M., Germuska, M., Xie, J., Chappell, M.A., Okell, T.W., Bright, M.G., Jezzard, P., 2012. Quantitative measurement of cerebral physiology using respiratory-calibrated MRI. Neuroimage 60, 582–591. https://doi.org/10.1016/j.neuroimage.2011.12.017.

Chen, J.J., Pike, G.B., 2009. BOLD-specific cerebral blood volume and blood flow changes during neuronal activation in humans. NMR Biomed. 22, 1054–1062. https://doi.org/10.1002/nbm.1411.

Dai, W., Garcia, D., De Bazelaire, C., Alsop, D.C., 2008. Continuous flow-driven inversion for arterial spin labeling using pulsed radio frequency and gradient fields. Magn. Reson. Med. 60, 1488–1497. https://doi.org/10.1002/mrm.21790.

Davis, T.L., Kwong, K.K., Weisskoff, R.M., Rosen, B.R., 1998. Calibrated functional MRI: mapping the dynamics of oxidative metabolism. Proc. Natl. Acad. Sci. U. S. A. 95, 1834–1839. https://doi.org/10.1073/pnas.95.4.1834.

Donahue, M.J., Faraco, C.C., Strother, M.K., Chappell, M. a, Rane, S., Dethrage, L.M., Hendrikse, J., Siero, J.C.W., 2014. Bolus arrival time and cerebral blood flow responses to hypercarbia. J. Cereb. Blood Flow. Metab. 34, 1243–1252. https://doi.org/10.1038/jcbfm.2014.81.

Donahue, M.J., Strother, M.K., Lindsey, K.P., Hocke, L.M., Tong, Y., deB Frederick, B., 2016. Time delay processing of hypercapnic fMRI allows quantitative parameterization of cerebrovascular reactivity and blood flow delays. J. Cereb. Blood Flow. Metab. 36, 1767–1779. https://doi.org/10.1177/0271678X15608643.

Duffin, J., Sobczyk, O., Crawley, A.P., Poublanc, J., Mikulis, D.J., Fisher, J.A., 2015. The dynamics of cerebrovascular reactivity shown with transfer function analysis. Neuroimage 114, 207–216. https://doi.org/10.1016/j.neuroimage.2015.04.029.

Duvernoy, H.M., 1981. Cortical blood vessels of the human brain. Brain Res. Bull. 7, 519–579.

Duvernoy, H.M., Delon, S., Vannson, J.L., 1981. Cortical blood vessels of the human brain. Brain Res. Bull. 7, 519–579. https://doi.org/10.1016/0361-9230(81)90007-1.

Faraci, F.M., Heistad, D.D., 1990. Regulation of large cerebral arteries and cerebral microvascular pressure. Circ. Res. 66, 8–17. https://doi.org/10.1161/01.RES.66.1.8.

Floyd, T.F., Clark, J.M., Gelfand, R., Detre, J. a, Ratcliffe, S., Guvakov, D., Lambertsen, C.J., Eckenhoff, R.G., 2003. Independent cerebral vasoconstrictive effects of hyperoxia and accompanying arterial hypocapnia at 1 ATA. J. Appl. Physiol. 95, 2453–2461. https://doi.org/10.1152/japplphysiol.00303.2003.

Frederick, B. deB., Nickerson, L.D., Tong, Y., 2012. Physiological denoising of BOLD fMRI data using Regressor Interpolation at Progressive Time Delays (RIPTiDe) processing of concurrent fMRI and near-infrared spectroscopy (NIRS). Neuroimage 60, 1913–1923. https://doi.org/10.1016/j.neuroimage.2012.01.140.

Germuska, M., Merola, A., Murphy, K., Babic, A., Richmond, L., Khot, S., Hall, J.E., Wise, R.G., 2016. A forward modelling approach for the estimation of oxygen extraction fraction by calibrated fMRI. Neuroimage 139, 313–323. https://doi.org/10.1016/j.neuroimage.2016.06.004.

Glodzik, L., Randall, C., Rusinek, H., de Leon, M.J., 2013. Cerebrovascular reactivity to carbon dioxide in Alzheimer's disease. J. Alzheimers. Dis. 35, 427–440. https://doi.org/10.3233/JAD-122011.

Grubb, R.L., Raichle, M.E., Eichling, J.O., Ter-Pogossian, M.M., 1974. The effects of changes in PaCO2 on cerebral blood volume, blood flow, and vascular mean transit time. Stroke 5, 630–639. https://doi.org/10.1161/01.STR.5.5.630.

Han, J.S., Abou-Hamden, A., Mandell, D.M., Poublanc, J., Crawley, A.P., Fisher, J.A., Mikulis, D.J., Tymianski, M., 2011. Impact of extracranial-intracranial bypass on cerebrovascular reactivity and clinical outcome in patients with symptomatic moyamoya vasculopathy. Stroke 42, 3047–3054. https://doi.org/10.1161/STROKEAHA.111.615955.

Herscovitch, P., Raichle, M.E., 1985. What is the correct value for the brain–blood partition coefficient for water? J. Cereb. Blood Flow. Metab. 5, 65–69. https://doi.org/10.1038/jcbfm.1985.9.

Jenkinson, M., Bannister, P., Brady, M., Smith, S., 2002. Improved optimization for the robust and accurate linear registration and motion correction of brain images. Neuroimage 17, 825–841. https://doi.org/10.1016/S1053-8119(02)91132-8.

Jenkinson, M., Smith, S., 2001. A global optimisation method for robust affine registration of brain images. Med. Image Anal. 5, 143–156. https://doi.org/10.1016/S1361-8415(01)00036-6.

Kennerley, A.J., Mayhew, J.E., Redgrave, P., Berwick, J., 2010. Vascular origins of BOLD and cbv fMRI signals: statistical mapping and histological sections compared. Open neuroimag. J. 4, 1–8 doi:1874-4400/10.

Kontos, H. a., Wei, E.P., Raper, a. J., Patterson, J.L., 1977. Local mechanism of CO2 action of cat pial arterioles. Stroke 8, 226–229. https://doi.org/10.1161/01.STR.8.2.226.

Leung, J., Dufin, J., Fisher, J.A., Kassner, A., 2016. MRI-based cerebrovascular reactivity using transfer function analysis reveals temporal group differences between patients with sickle cell disease and healthy controls. NeuroImage Clin. 12, 624–630. https://doi.org/10.1016/j.nicl.2016.09.009.

Lindauer, U., Vogt, J., Schuh-Hofer, S., Dreier, J.P., Dirnagl, U., 2003. Cerebrovascular vasodilation to extraluminal acidosis occurs via combined activation of ATP-sensitive and Ca2+-activated potassium channels. J. Cereb. Blood Flow. Metab. 23, 1227–1238. https://doi.org/10.1097/01.WCB.0000088764.02615.B7.

Liu, P., Welch, B.G., Li, Y., Gu, H., King, D., Yang, Y., Pinho, M., Lu, H., 2017. Multiparametric imaging of brain hemodynamics and function using gas-inhalation MRI. Neuroimage 146, 715–723. https://doi.org/10.1016/j.neuroimage.2016.09.063.

Lu, H., Clingman, C., Golay, X., Van Zijl, P.C.M., 2004. Determining the longitudinal relaxation time (T1) of blood at 3.0 tesla. Magn. Reson. Med. 52, 679–682. https://doi.org/10.1002/mrm.20178.

Ma, Y., Berman, A.J.L., Pike, G.B., 2014. The effect of dissolved oxygen on relaxation rates of blood plasma. In: Proceedings 22nd Scientific Meeting International Society for Magnetic Resonance in Medicine, p. 3099.

Mark, C.I., Pike, G.B., 2012. Indication of BOLD-specific venous flow-volume changes from precisely controlled hyperoxic vs. hypercapnic calibration. J. Cereb. Blood Flow. Metab. 32, 709–719. https://doi.org/10.1038/jcbfm.2011.174.

Mazziotta, J., Toga, A., Evans, A., Fox, P., Lancaster, J., Zilles, K., Woods, R., Paus, T., Simpson, G., Pike, B., Holmes, C., Collins, L., Thompson, P., MacDonald, D., Iacoboni, M., Schormann, T., Amunts, K., Palomero-Gallagher, N., Geyer, S., Parsons, L., Narr, K., Kabani, N., Goualher, G. Le, Boomsma, D., Cannon, T., Kawashima, R., Mazoyer, B., 2001. A probabilistic atlas and reference system for the human brain: international Consortium for Brain Mapping (ICBM). Philos. Trans. R. Soc. Lond. B Biol. Sci. 356, 1293–1322. https://doi.org/10.1098/rstb.2001.0915.

Moody, D.M., Bell, M.A., Challa, V.R., 1990. Features of the cerebral vascular pattern that predict vulnerability to perfusion or oxygenation deficiency: an anatomic study. Am. J. Neuroradiol. 11, 431–439 doi:Thesis #26.

Ogawa, S., Lee, T.M., Kay, A.R., Tank, D.W., 1990. Brain magnetic resonance imaging with contrast dependent on blood oxygenation. Proc. Natl. Acad. Sci. U. S. A. 87, 9868–9872. https://doi.org/10.1073/pnas.87.24.9868.

Posse, S., Wiese, S., Gembris, D., Mathiak, K., Kessler, C., Grosse-Ruyken, M.L., Elghahwagi, B., Richards, T., Dager, S.R., Kiselev, V.G., 1999. Enhancement of BOLD-contrast sensitivity by single-shot multi-echo functional MR imaging. Magn. Reson. Med. 42, 87–97. https://doi.org/10.1002/(SICI)1522-2594(199907)42, 1<87::AID-MRM13>3.0.CO;2-O.

Poublanc, J., Crawley, A.P., Sobczyk, O., Montandon, G., Sam, K., Mandell, D.M., Dufort, P., Venkatraghavan, L., Duffin, J., Mikulis, D.J., Fisher, J. a, 2015. Measuring cerebrovascular reactivity: the dynamic response to a step hypercapnic stimulus. J. Cereb. Blood Flow. Metab. 1–11. https://doi.org/10.1038/jcbfm.2015.114.

Rostrup, E., Law, I., Blinkenberg, M., Larsson, H.B., Born, a P., Holm, S., Paulson, O.B., 2000. Regional differences in the CBF and BOLD responses to hypercapnia: a combined PET and fMRI study. Neuroimage 11, 87–97. https://doi.org/10.1006/nimg.1999.0526.

Sam, K., Small, E., Poublanc, J., Han, J., Mandell, D., Fisher, J., Crawley, A., Mikulis, D., 2014. Reduced contralateral cerebrovascular reserve in patients with unilateral steno-occlusive disease. Cerebrovasc. Dis. 38, 94–100.

Severinghaus, J.W., 1979. Simple, accurate equations for human blood O2 dissociation computations. J. Appl. Physiol. 46, 599–602.

Sobczyk, O., Battisti-Charbonney, A., Fierstra, J., Mandell, D.M., Poublanc, J., Crawley, A.P., Mikulis, D.J., Duffin, J., Fisher, J.A., 2014. A conceptual model for CO2-induced redistribution of cerebral blood flow with experimental confirmation using BOLD MRI. Neuroimage 92, 56–68. https://doi.org/10.1016/j.neuroimage.2014.01.051.

Sobczyk, O., Battisti-charbonney, A., Poublanc, J., Crawley, A.P., Sam, K., Fierstra, J., Mandell, D.M., Mikulis, D.J., Duffin, J., Fisher, J.A., 2015. Assessing cerebrovascular reactivity abnormality by comparison to a reference atlas. J. Cereb. Blood Flow. Metab. 35, 213–220. https://doi.org/10.1038/jcbfm.2014.184.

Tajima, Y., Takuwa, H., Nishino, A., Matsuura, T., Kawaguchi, H., Ikoma, Y., Taniguchi, J., Seki, C., Masamoto, K., Kanno, I., Saeki, N., Ito, H., 2014. Cerebral hemodynamic response to acute hyperoxia in awake mice. Brain Res. 1557, 155–163. https://doi.org/10.1016/j.brainres.2014.01.053.

Thomas, B.P., Liu, P., Park, D.C., van Osch, M.J.P., Lu, H., 2014. Cerebrovascular reactivity in the brain white matter: magnitude, temporal characteristics, and age effects. J. Cereb. Blood Flow. Metab. 34, 242–247. https://doi.org/10.1038/jcbfm.2013.194.

Tong, Y., Bergethon, P.R., Frederick, B. deB., 2011. An improved method for mapping cerebrovascular reserve using concurrent fMRI and near-infrared spectroscopy with Regressor Interpolation at Progressive Time Delays (RIPTiDe). Neuroimage 56, 2047–2057. https://doi.org/10.1016/j.neuroimage.2011.03.071.

Wang, J., Alsop, D.C., Song, H.K., Maldjian, J.A., Tang, K., Salvucci, A.E., Detre, J.A., 2003. Arterial transit time imaging with flow encoding arterial spin tagging (FEAST). Magn. Reson. Med. 50, 599–607. https://doi.org/10.1002/mrm.10559.

Woolrich, M.W., Chiarelli, P., Gallichan, D., Perthen, J., Liu, T.T., 2006. Bayesian inference of hemodynamic changes in functional arterial spin labeling data. Magn. Reson. Med. 56, 891–906. https://doi.org/10.1002/mrm.21039.

Wu, W., Buxton, R.B., Wong, E.C., 2007. Vascular space occupancy weighted imaging with control of residual blood signal and higher contrast-to-noise ratio. IEEE Trans. Med. Imaging 26, 1319–1327. https://doi.org/10.1109/TMI.2007.898554.

Xu, F., Liu, P., Pascual, J.M., Xiao, G., Lu, H., 2012. Effect of hypoxia and hyperoxia on cerebral blood flow, blood oxygenation, and oxidative metabolism. J. Cereb. Blood Flow. Metab. 32, 1909–1918. https://doi.org/10.1038/jcbfm.2012.93.

Zhang, X., Petersen, E.T., Ghariq, E., De Vis, J.B., Webb, a G., Teeuwisse, W.M., Hendrikse, J., van Osch, M.J.P., 2012. In vivo blood T(1) measurements at 1.5 T, 3 T, and 7 T. Magn. Reson Med. 0, 1–5. https://doi.org/10.1002/mrm.24550.

Zhang, Y., Brady, M., Smith, S., 2001. Segmentation of Brain MR Images through a Hidden Markov Random Field Model and the Expectation-maximization Algorithm, vol. 20, pp. 45–57.